Supporting Information

Efficient mechanical modulation of the phonon thermal conductivity of Mo_6S_6 nanowires

Ke Xu,[1, #] Shichen Deng,[2, #] Ting Liang,[3] Xuezheng Cao,[1] Meng Han,[3] Xiaoliang Zeng,[3] Zhisen Zhang,[1] Nuo Yang,[2, a)] and Jianyang Wu[1, 4, b)]

[1]Department of Physics, Research Institute for Biomimetics and Soft Matter, Jiujiang Research Institute and Fujian Provincial Key Laboratory for Soft Functional Materials Research, Xiamen University, Xiamen 361005, PR China

[2]State Key Laboratory of Coal Combustion, and School of Energy and Power Engineering, Huazhong University of Science and Technology (HUST), Wuhan, 430074 PR China

[3]Shenzhen Institute of Advanced Electronic Materials, Shenzhen Institutes of Advanced Technology, Chinese Academy of Sciences, Shenzhen 518055, PR China

[4]NTNU Nanomechanical Lab, Norwegian University of Science and Technology (NTNU), Trondheim 7491, Norway

[#] These authors contributed equally to this work.
[a)] Electronic mail: nuo@hust.edu.cn (N. Y.)
[b)] Electronic mail: jianyang@xmu.edu.cn (J. W.)

1. Molecular Models of Deformed Mo_6S_6 Nanowire

Table S1 lists the detailed information of both stretched and twisted Mo_6S_6 nanowires. All the investigated atomic models of Mo_6S_6 nanowires are composed of identical number of atoms (6000). However, as a result of axial elongation and twisting deformation, they show different lattice constants in axial direction. Figure S1 shows the detailed structural information of Mo_6S_6 nanowires subjected to axial tension and torsional strain.

Table S1 Structural information of mechanically-deformed Mo_6S_6 nanowires

Stretched Nanowires					No. 6000			
Tensile Strain (m/m)	0.0	0.005	0.01	0.015	0.02	0.025	0.03	0.04
Axial Length $\mathbf{C_1}$ (Å)	4.60	4.63	4.65	4.67	4.69	4.72	4.74	4.79
Twisted Nanowires					No. 6000			
Torsional Strain (°/nm)	0.0	10.5	21.0	31.7	42.4	53.3	64.2	75.2
Axial Length $\mathbf{C_1}$ (Å)	4.60	4.58	4.57	4.55	4.53	4.51	4.49	4.47

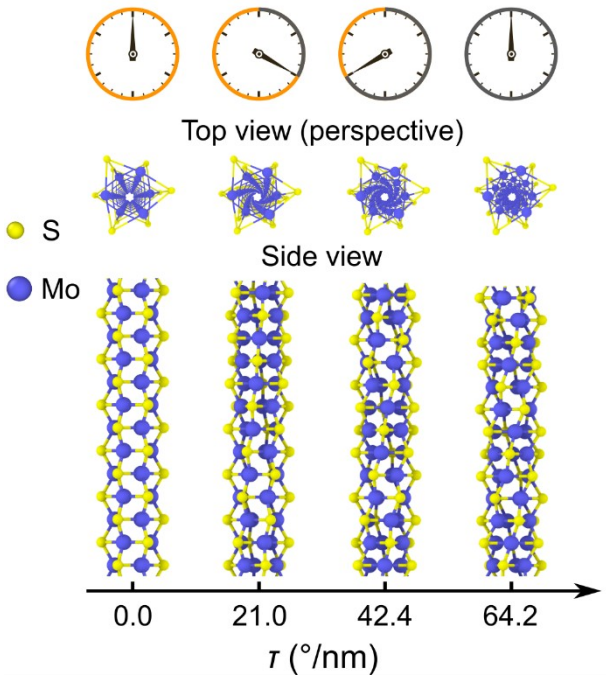

Figure S1 Schematic of Mo_6S_6 nanowire subjected to four different torsional strains (τ) that are 0.0, 21.0, 42.4 and 64.2°/nm, respectively. For top schematic, the clockwise rotation is used to indicate the

twisting angles of Mo_6S_6 nanowire. For bottom-viewed atomic models, the Mo and S atoms in Mo_6S_6 nanowire are yellow- and blue-colored for clarification.

2. Methodology

2.1 Settings of NEMD simulations

The detailed setting parameters of all NEMD simulations are listed in Table S2. ReaxFF potential is a powerful tool to study a wide range of systems[1-4]. On the other hand, the popular forcefields of Mo-S type REBO[5] and SW[6] are tested, While, both Mo-S type REBO[5] and SW forcefields are not able to stabilize Mo_6S_6 nanowire. A small timestep of 0.2 fs is adopted to perform the NEMD. For Mo-S systems, ReaxFF forcefield was also adopted to study the thermal[7, 8] and mechanical properties[9, 10]. The simulation procedure is summarized as follows. After minimization, the NPT ensemble is used to relax the Mo_6S_6 nanowire structure for 1 ns. Then, except for the thermostat regions, the rest of the system is simulated by NVE ensemble for 8 ns to reach the steady state. Finally, a longer simulation using NVE ensemble is performed for 2 ns to record and average the temperature and heat flux. Here, we use a more efficient NEMD method with fixed boundaries, as shown in Figure S2b.

Table S2. NEMD simulation details

Method	Non-Equilibrium molecular dynamics		
Parameters			
Potential	ReaxFF	**Time step**	0.2 fs
Thermostat	Langevin	**Temperature difference**	30 K
Simulation process			
Ensemble	**Setting**		**Purpose**
NVT	Boundary condition	x, y, z: p, p, f	Relax structure
	Runtime	1 ns	
NVE	Boundary condition	x, y, z: p, p, f	Reach steady state
	Runtime	8 ns	
NVE	Boundary condition	x, y, z: p, p, f	Reach information
	Runtime	2 ns	
Recorded physical quantity			

Temperature	$\langle E \rangle = \sum_{i=1}^{N} \frac{1}{2} m^i v_i^2 = \frac{3}{2} N k_B T$
Heat flux	$J = \frac{\Delta E_{in} + \Delta E_{out}}{2\Delta t}$
Thermal conductivity	$\kappa = -\frac{J}{A\nabla T} = -\frac{JL}{A\Delta T}$

2.2 NEMD method

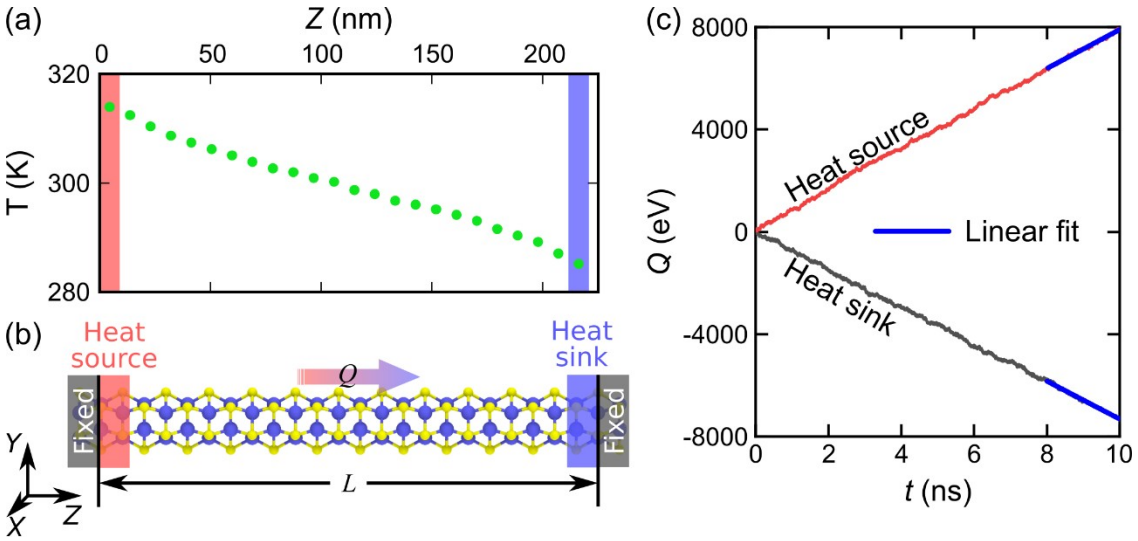

Figure S2 (a) Steady-state temperature profile in the Mo_6S_6 system. (b) The axial direction of the tube is the *z* direction, and the heat flow (Q) transfer is imposed in this direction. (c) The energy of the source and sink thermostat as a function of the time in steady state.

3 The phonon thermal conductivity

3.1 Phonon transmission spectra and Accumulated thermal conductivity

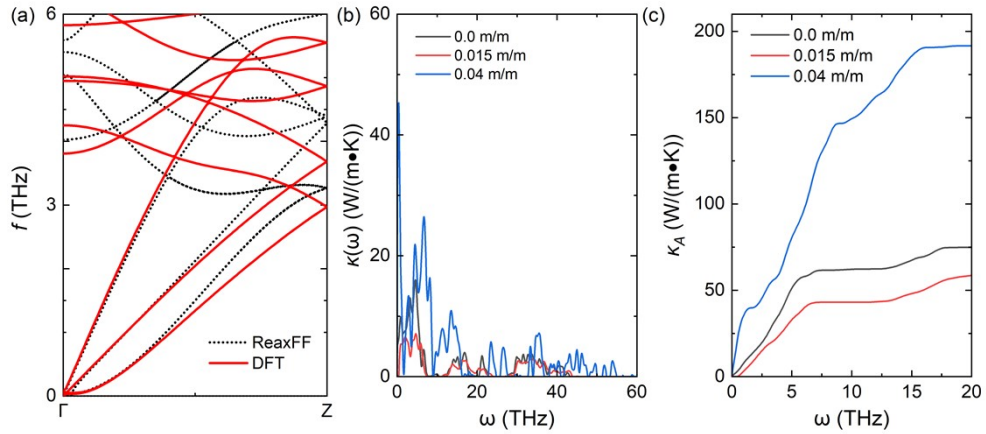

Figure S3. (a) Phonon dispersion predicted by ReaxFF-based MD calculations and DFT calculations ($\omega<\omega^{A}_{max}$, ω^{A}_{max}=6 THz). (b) Phonon transmission spectra ($\kappa(\omega)$) of Mo_6S_6 nanowire with frequency (ω) range at 0-60 THz. (c) Accumulated thermal conductivity (κ_A) of Mo_6S_6 nanowire with frequency (ω) range at 0-20 THz.

Here, the spectral thermal conductivity of Mo_6S_6 NW is calculated from the transmission coefficient, as shown in Figure S3(a). As is indicated, the thermal conductivity of Mo_6S_6 NW subjected to zero strain is largely contributed by the low-frequency region. Such case is also identified as Mo_6S_6 NW is stretched and twisted, as shown in the Figure S3(b). Therefore, the dependence of the thermal conductivity on mechanical strains is dictated by low-frequency contributions.

To verify the accuracy of our ReaxFF-based MD results, the phonon spectrum is also predicted by density functional theory (DFT) calculations, as shown in the Figure S3(c). The black dashed lines are the phonon dispersion relation curves of Mo_6S_6 NW at zero strain obtained from a lattice dynamic program Phonopy[11]. The phonon dispersion with DFT calculations was extracted from VASP[12] (Vienna Ab initio Simulation Package), in which the PBE was used for the exchange-correlation

functional, and self-consistent calculation was performed with a cutoff energy of 600 eV and a force convergence criterion of 10^{-7} eV/Å. By comparison, it is found that phonon spectrogram of Mo_6S_6 NW in the low-frequency region predicted by ReaxFF-based MD calculations are in good agreement with that by DFT calculations. Given that the thermal conductivity of Mo_6S_6 NW by ReaxFF-based MD simulations is largely contributed by the low-frequency region. Therefore, the thermal conductivity of Mo_6S_6 NW by ReaxFF-based MD calculations is reliable.

3.2 Phonon thermal conductivity and *v*DOS of full frequency.

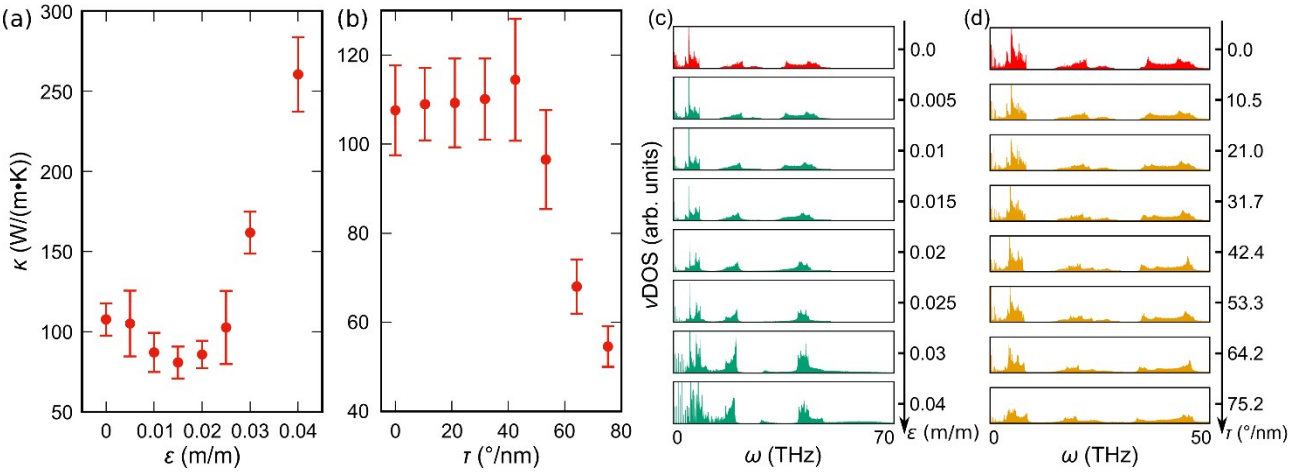

Figure S4 (a) and (b) Variations in the phonon thermal conductivity (*v*DOS) of Mo_6S_6 nanowire with tensile (ε) and torsional (τ) strains, respectively. (c) and (d) *v*DOS of isolated Mo_6S_6 nanowire subjected to different tensile and torsional strains.

As shown in the Figures S3(c-d), the upper-bound frequency is increased, for example, it reaches about 65 THz at axial tension strain of 0.04. Such strain-induced transition change in the vDOS spectra explains the crossover of phonon thermal conductivity in Mo_6S_6 NW.

3.3 Size effect and three-phonon scattering

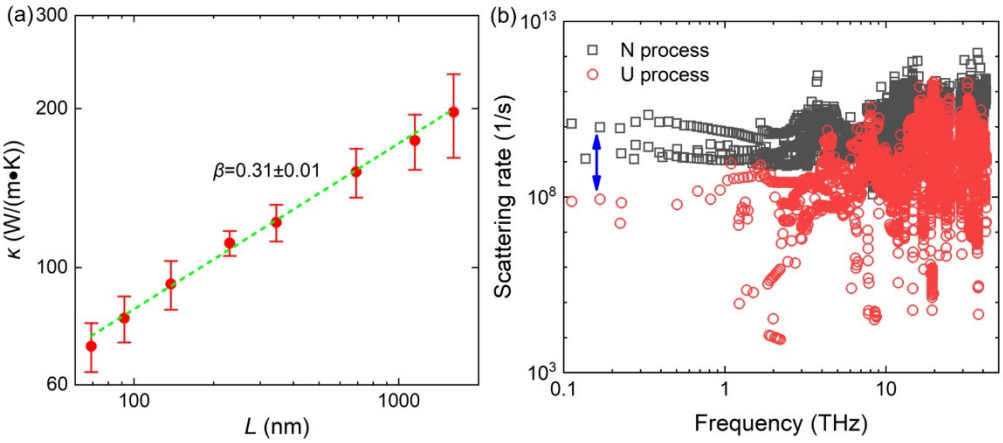

Figure S5. (a) Thermal conductivity (κ) for Mo_6S_6 nanowire at 300 K with different lengths (L) from the NEMD simulations. (b) Three-phonon scattering rates in Mo_6S_6 nanowires subjected to zero strain as a function of phonon frequency, including Normal and Umklapp processes.

It is well known that there is size effect on the thermal conductivity of low-dimensional materials. As shown in the Figure S5a, the size effect of thermal conductivity of Mo_6S_6 NW is also examined. Figure R4 shows the variation in the thermal conductivity of Mo_6S_6 NW with axial length. It is revealed that the thermal conductivity of Mo_6S_6 NW follows $\kappa \propto L^{\beta}$, and here $\beta = 0.31$. This suggests that the thermal conductivity of Mo_6S_6 NW follows one-dimensional (1D) nonlinear lattice model. Our results are in good agreement with previous predictions of 1D nanostructure, namely, the thermal conductivity of 1D materials is length dependent[13, 14]. In our study, Mo_6S_6 NW with finite axial length of 200 nm is generated to reveal the role of tension and torsion strains on the thermal conductivity.

As shown in Figure S5b, we calculated the three-phonon scattering rates of the Mo_6S_6 NW. The three-phonon scattering rates is calculated by PHONO3PY[15] and includes the Normal process and Umklapp process. The third-order interatomic force constants, with an atomic displacement of 0.03 Å,

is calculated from the finite difference method. As is indicated, the normal (N) process is around two orders of magnitudes stronger than the Umklapp (U) process in low-frequency range (< 1 THz).

3.4 Phonon dispersion relationship

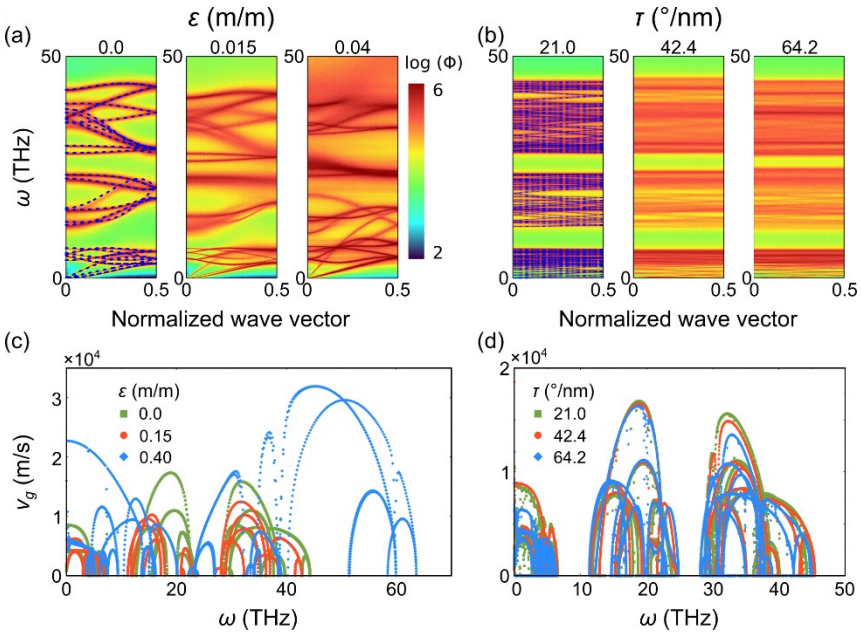

Figure S6 (a) and (b) Phonon dispersion relationship of isolated Mo_6S_6 nanowire subjected to three critical tensile (ε) and torsional (τ) strains, respectively. (c) and (d) Phonon group velocity (v_g) as a function of frequency (ω) for isolated Mo_6S_6 nanowire under three critical tensile (ε) and torsional (τ) strains, respectively.

The blue dashed lines are the phonon dispersion relation curves of Mo_6S_6 NW at zero strain obtained from a lattice dynamic program Phononpy[11]. As shown in the Figure S4, the highest frequency is enlarged to about 65 THz, but at high frequency region, the SED curves are not able to distinguish, indicating severe phonon scattering. The high frequency phonons cover a wide frequency range, and the group velocity is tripled, thereby resulting in increase in the phonon thermal conductivity.

4. Bond length distribution

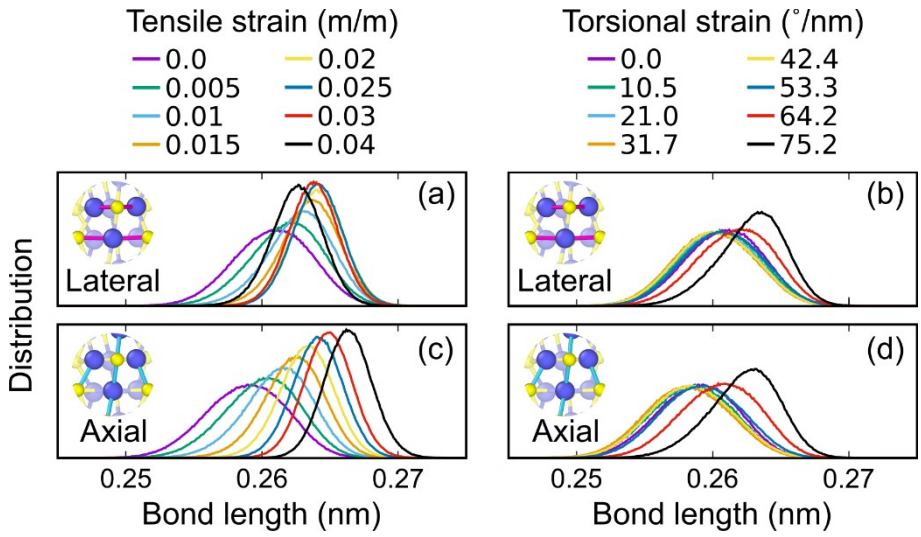

Figure S7 (a) and (c) Distribution of bond length of unique Mo-S bond that makes 0° and 90° angles to the axial direction of wire as the Mo_6S_6 nanowire is subjected to different tension strains (ε), respectively. (a) and (c) Distribution of bond length of unique Mo-S bond that makes 0° and 90° angles to the axial direction of wire as the Mo_6S_6 nanowire is subjected to different torsional strains (τ) respectively.

References

1. N. C. Osti, M. Naguib, A. Ostadhossein, Y. Xie, P. R. C. Kent, B. Dyatkin, G. Rother, W. T. Heller, A. C. T. van Duin, Y. Gogotsi and E. Mamontov, *ACS Appl. Mater. Interfaces*, 2016, **8**, 8859-8863.
2. A. Ostadhossein, E. D. Cubuk, G. A. Tritsaris, E. Kaxiras, S. Zhang and A. C. T. van Duin, *Phys. Chem. Chem. Phys.*, 2015, **17**, 3832-3840.
3. K. Yoon, A. Ostadhossein and A. C. T. van Duin, *Carbon*, 2016, **99**, 58-64.
4. M. M. Islam, A. Ostadhossein, O. Borodin, A. T. Yeates, W. W. Tipton, R. G. Hennig, N. Kumar and A. C. T. van Duin, *Phys. Chem. Chem. Phys.*, 2015, **17**, 3383-3393.
5. T. Liang, S. R. Phillpot and S. B. Sinnott, *Phys. Rev. B*, 2009, **79**, 245110.
6. J.-W. Jiang, *Nanotechnology*, 2015, **26**, 315706.
7. B. Mortazavi, R. Quey, A. Ostadhossein, A. Villani, N. Moulin, A. C. T. van Duin and T. Rabczuk, *Applied Materials Today*, 2017, **7**, 67-76.
8. H. Farahani, A. Rajabpour, M. Khanaki and A. Reyhani, *Comput. Mater. Sci.*, 2018, **142**, 1-6.
9. B. Mortazavi, A. Ostadhossein, T. Rabczuk and A. C. T. van Duin, *Phys. Chem. Chem. Phys.*, 2016, **18**, 23695-23701.
10. A. Ostadhossein, A. Rahnamoun, Y. Wang, P. Zhao, S. Zhang, V. H. Crespi and A. C. T. van Duin, *J. Phys. Chem. Lett.*, 2017, **8**, 631-640.
11. A. Togo and I. Tanaka, *Scripta Mater.*, 2015, **108**, 1-5.

12. G. Kresse and J. Furthmüller, *Phys. Rev. B*, 1996, **54**, 11169-11186.
13. J.-S. Wang and B. Li, *Phys. Rev. Lett.*, 2004, **92**, 074302.
14. N. Yang, G. Zhang and B. Li, *Nano Today*, 2010, **5**, 85-90.
15. A. Togo, L. Chaput and I. Tanaka, *Phys. Rev. B*, 2015, **91**, 094306.